



Simulated solar light-driven photothermal preferential oxidation of carbon monoxide in H₂-rich streams over fast-synthesized CuCeO_{2-x} nanorods

Xiaolin Guo^{a,1}, Wangxiang Ye^{a,1}, Zi'ang Chen^a, Ang Zhou^a, Dingfeng Jin^a, Tingli Ma^{a,b,*}

^a College of Materials and Chemistry, China Jiliang University, Hangzhou 310018, PR China

^b Graduate School of Life Science and Systems Engineering, Kyushu Institute of Technology, 2-4 Hibikino, Wakamatsu, Kitakyushu, Japan

ARTICLE INFO

Keywords:

Hydrogen purification
Preferential oxidation of CO
Photothermal catalysis
CuCeO_{2-x} nanorods
Solar light-driven

ABSTRACT

Aiming for purification the trace amount of CO in H₂-rich streams with reduced energy consumption and low cost, solar-driven photothermal preferential oxidation of carbon monoxide on the non-precious metal oxide catalyst is proposed in this work. Cu doped CuCeO_{2-x} nanorods catalysts were synthesized with a fast and simple coprecipitation method at the room temperature, which shows high CO oxidation activity in photothermal preferential oxidation of CO (CO-PROX) under UV-Vis-IR light irradiation. Rely on the various characterization methods such as UV-Vis-IR diffuse reflection spectrum (UV-Vis-IR DRS), photoluminescence spectrum (PL), transient photocurrent test, HRTEM, XRD, XPS, UV-Raman and H₂-TPR, the optical and chemical properties of the CuCeO_{2-x} nanorods catalysts were uncovered. The photothermal catalytic activity of CuCeO_{2-x} nanorods doped with 10 wt% Cu reaches to 90% CO conversion under Xe lamp illumination (2.5 suns), and the solar driven photothermal CO-PROX reaction on CuCeO_{2-x} nanorods were proposed to be proceeded by the light-to-thermal conversion and subsequently to drive a thermal catalytic process. The catalytic performance of CuCeO_{2-x} nanorods in photothermal CO-PROX is closely related to the photo-to-thermal conversion efficiency and Cu-Ce synergetic interaction of CuCeO_{2-x} nanorods catalyst. The introduction of CuO_x greatly broaden the optical absorption range and promotes the light absorption capacity of ceria nanorods, which induces the catalyst with high photo-to-thermal conversion capability. Moreover, the optimal copper dopant benefits to enhance the Cu-Ce synergetic interaction and accelerate the oxidation reaction taking place at low temperature. CuCeO_{2-x} nanorods catalyst shows promising competitive activity and ultra-low cost compared with the noble-based catalyst for the purification of hydrogen streams by the clean and eco-friendly sunlight sources.

1. Introduction

Hydrogen is a clean secondary energy carrier. Proton exchange membrane fuel cell (PEMFC) using hydrogen as fuel has the advantages of high energy efficiency, low operating temperature and zero emissions, and is an ideal energy source for hydrogen fuel cell vehicles. At present, the industrial production of hydrogen is mainly derived from the reforming reaction of fossil fuels (about 90% of the total production), and the produced hydrogen-rich hydrogen contains about 10% (V/V) of CO. After the water-gas shift reaction, the concentration of CO in hydrogen-rich hydrogen is still as high as 2000 ppm, which cannot meet the application requirements of proton exchange membrane fuel cells. As an important part of the fuel cell-grade hydrogen production and purification process, CO Preferential Oxidation (CO-PROX) can

remove the CO concentration in the rich hydrogen to below 100 ppm, which is considered as a very economical and effective method for deep purification of trace CO in rich hydrogen. A wide variety of promising catalysts based on supported noble metals (e.g., Au and Pt) [1–4] and transition metal oxides (e.g., CuO-CeO₂ and Co₃O₄) [5–10] have been investigated for the thermal oxidation of CO, which mainly focus on the thermal catalysis of CO-PROX.

More recently, simulated sunlight with UV-Vis-IR irradiation has also been proposed to replace the thermal condition to perform the CO oxidation reaction, avoiding the use of thermal sources to input energy into the system. A series of work on Au-based catalyst photocatalytic CO selective oxidation have been carried out by the research group of X. Fu, and W. Dai, including PANI-assisted Au-TiO₂, Cu-modified Au-TiO₂, Au/ZIF-8-TiO₂, Au-ZnCo₂O₄, Au-TiO₂-C₃N₄ and other catalysts [11–15] for

* Corresponding author.

E-mail address: matngli123@cjl.u.edu.cn (T. Ma).

¹ These authors contributed equally to this work

the photocatalytic CO-PROX under visible light. They found that Au nanoparticles produced plasmon resonance on the local surface of TiO_2 , which induces the migration of excited electrons, increases the surface electron density of Au- TiO_2 , and promotes the oxidation of CO. Moreover, the protonation of the N atom in the conductive polymer poly PANI causes the dissociated H at the Au site to overflow into the PANI, inhibiting the H_2 oxidation reaction. For the Cu-modified Au- TiO_2 catalyst, the CuO shell generates photoexcitation under visible light irradiation, and enhances the Au, TiO_2 and CuO sites. The electron transfer between Au and the carrier surface electron density was increased, and the adsorption and activation of CO and O_2 were accelerated. In addition, the research group of Elisa Moretti has also performed a series of research work on the selective oxidation of CO on Au-based catalysts, such as Au-Cu-SBA, Au- TiO_2 nanorods, Au-transition metal oxide-sea foam stones [16–18] under simulated sunlight. The research results also confirmed that the excitation of the local surface plasmon resonance of Au nanoparticles, which reduces the electron-hole recombination of photo-generated charge carriers and promotes the photocatalytic CO oxidation on Au- TiO_2 . However, for the series of Au-based catalyst, the CO conversion rate increased significantly under visible light irradiation at room temperature, but its CO oxidation selectivity decreased significantly, which means that the light stimulated the oxidation reaction of CO and H_2 at the same time. And their high costs make them unfavorable for future utilization.

For semiconductor oxides (especially black or dark-colored catalysts) such as CuO, Co_3O_4 and MnO_2 et. al, due to the photothermal effect, the surface temperature rises instantaneously under light, which causes the electron excitation and relaxation, and enhanced thermal radiation at the same time. For instance, Zhao et al. [19] synthesized CuO mesoporous nanosheets (CuO-MNS) and applied it to the photothermal catalytic CO oxidation reaction. They found that under UV-Vis-IR radiation, the photothermal catalytic activity of CuO-MNS is the photocatalytic activity at light intensity of $475.7 \text{ mW}\cdot\text{cm}^{-2}$ is 331 times higher than conventional thermal catalytic process, and it also shows effective photothermal catalytic activity even under $\lambda > 830 \text{ nm}$ infrared light. UV-Vis-IR radiation promotes the re-oxidation of the reduced CuO-MNS and the photoactivation greatly enhanced the light-driven thermal catalytic activity of CuO-MNS. Xu [20] et al. designed and synthesized CuO hollow spheres with a multi-level structure. The results show that the multi-level structure greatly enhances its light absorption and light-to-heat conversion capabilities. The local temperature of its surface is as high as 200°C under the sunlight at room temperature. The photothermal catalytic CO oxidation reaction rate at room temperature is 20 times higher than the thermal catalysis at 240°C .

CeO_2 is widely applied as the support in the thermal oxidation catalysis, on account of its flexible lattice oxygen mobility and abundant oxygen vacancy that could afford sufficient oxygen species during the catalytic process. Moreover, CeO_2 is an n-type semiconductor with a band gap of 3.1 eV, and its light absorption range can be extended to about 500 nm by inducing the generation of Ce^{3+} and oxygen defects. CeO_2 is usually regarded as a combination of n-type semiconductors and oxygen ion conductors because of its very high tolerance for oxygen ion defects (VO). Therefore, the photocurrent response of the CeO_2 electrode increased with increasing temperature under the excitation of UV-Vis-IR. Zhao et al. [21] directly coated CeO_2 nanorods on the surface of the mercury lamp, and the surface temperature of the sample reached approximately 240°C . Its photothermal catalytic rate constant for photothermal catalytic oxidation activity of benzene is 9.2 times higher than that at room temperature, and 6.3 times higher than the thermal catalytic rate constant in a dark environment at 240°C . Therefore, considering the excellent photothermal conversion of CuO, the semi-conductive and oxygen ion conductive property of CeO_2 , and the as-reported strong synergy interaction between CuO and CeO_2 , it is essential to develop a composite CuO- CeO_2 catalyst and apply them in the photothermal catalysis of CO-PROX, which is promising to be considered as the clean, eco-friendly and high-efficient method for

removing the trace CO in the hydrogen-rich streams.

Herein, Cu doped CuCeO_{2-x} nanorods catalysts were synthesized with a fast and simple coprecipitation method at the room temperature, which shows relatively high CO conversion in photothermal preferential oxidation of CO in H_2 -rich streams under UV-Vis-IR light irradiation. Rely on the various characterization methods such as UV-Vis-IR DRS, PL, transient photocurrent test, HRTEM, XRD, XPS, UV-Raman and H_2 -TPR, the chemical and optical properties of the CuCeO_{2-x} nanorods catalysts were uncovered. CuCeO_{2-x} nanorods catalyst shows promising competitive activity and ultra-low cost compared with the noble-based catalyst for the purification of hydrogen streams by the clean and eco-friendly sunlight sources.

2. Experimental section

2.1. Materials

The reagents are all AR analytical reagents, without further purification before use. $\text{Ce}(\text{NO}_3)_3\cdot 6\text{H}_2\text{O}$, NaOH, absolute ethanol, concentrated hydrochloric acid, and quartz sand were purchased from Shanghai Maclean Biochemical Technology Co., Ltd., and CuCl was purchased from Shanghai Aladdin Biochemical Technology Co., Ltd. The solutions used in this article are all prepared with ultrapure water.

2.2. Synthesis

The CuCeO_{2-x} nanorods catalyst is prepared by one step coprecipitation method. Firstly, a certain amount of CuCl was dissolved in 5 mL concentrated hydrochloric acid, then 8 mmol $\text{Ce}(\text{NO}_3)_3\cdot 6\text{H}_2\text{O}$ was added into the solution, and the mixture solution was stirring magnetically until it is fully dissolved to form a dark green solution. At the same time, 140 mL of NaOH solution (38.4 g) was prepared. After cooled to room temperature, the NaOH solution was added to the hydrochloric acid solution of CuCl and $\text{Ce}(\text{NO}_3)_3$ under vigorous stirring, followed by continuous stirring for 30 min to form a brownish yellow suspension. The above steps are carried out under the protection of a nitrogen atmosphere at 30°C . After the reaction, the suspension was centrifuged, washed alternately with ethanol and deionized water to neutral, dried at 80°C overnight and then calcined at 500°C for 2 h. The obtained CuCeO_{2-x} nanorods with different copper content of 3%, 7%, 10% and 13% (the content percentage means the mass percentage of Cu/(CuO+ CeO_2)) were marked as 3CuCeO_x, 7CuCeO_x, 10CuCeO_x, and 13CuCeO_x, respectively. In addition, pure CeO_2 was prepared as a control sample according to the above process.

2.3. Catalyst characterization

The HRTEM images of the sample were characterized by FEI Tecnai G2 F20 transmission electron microscope (working voltage 200 kV). A small amount of sample was grinded in a mortar, then dispersed in absolute ethanol and ultrasonic for 30 min. After setting for 2 h, a small amount of suspension was dropwise to the ultra-thin carbon film copper mesh. After drying naturally, the copper mesh carrying the sample was put in the electron microscope gun, and placed into the electron microscope pretreatment chamber to a certain degree of vacuum for testing. The model of the energy spectrometer is OXFORD X-max 80 T. EDX elemental distribution mapping are obtained by FEI Talos F200S transmission electron microscope. The sample was loaded with molybdenum mesh, and the other preparation details were consistent with HRTEM.

The elemental composition of the sample was determined by PerkinElmer NexION 300X inductively coupled plasma mass spectrometer. The pretreatment process of the sample is as follows: 4 mL nitric acid is added to 6 mL water for dilution, then 30 mg sample is put into dilute nitric acid and heated at 180°C for 24 h.

The X-ray diffraction pattern of the sample was obtained by a

SmartLabSE X-ray diffractometer from Rigaku Corporation, Japan. The scan step size was 0.02° and the scan range was $10\text{--}90^\circ$. The XRD patterns were Rietveld refined using the Maud software. The method of refining crystallite size and morphology was on the basis of an anisotropic size function and Popa rules that ascribes the broadening of the crystallite size to a linear combination of spherical harmonic functions were utilized.

The X-ray photoelectron spectroscopy of the catalyst was obtained on the Thermo Scientific K-Alpha⁺ X-ray photoelectron spectrometer system. The Al K α micro-focus monochromatic source was adopted as X-ray source to achieve high-performance data acquisition (72 W) at low power. When the vacuum degree of the chamber is $\leq 2 \times 10^{-7}$ mbar, the energy spectrum of each element is calibrated with the surface pollution C1s (284.8 eV) as the standard. Smart model in Avantage software was used as baseline for the fitting of XP spectra.

The N₂ adsorption and desorption isotherm curves of the sample were measured using a TriStarII 3020 (Micromeritics Inc.) automatic physicochemical adsorption instrument at the temperature of liquid nitrogen (-196°C). The samples were pretreated at 200°C for 4 h in a high vacuum environment. The specific surface area of the sample is calculated using the Barrett-Emmett-Teller (BET) formula, and the pore volume and pore size distribution are calculated according to the Barrett-Joyner-Halenda (BJH) model.

The temperature-programmed hydrogen reduction test (H₂-TPR): 50 mg of the sample with a particle size of 60–80 mesh was put into a quartz

U-shaped tube and pretreated at 300°C for 30 min under nitrogen atmosphere. After the sample is cooled to room temperature, the nitrogen gas was switched to 5% H₂/Ar mixed gas (40 mL/min), and the temperature was programmed raised with a rate of $10^\circ\text{C}/\text{min}$ after the baseline is stable. The H₂ concentration is monitored by the thermal conductivity detector (TCD).

The Raman spectra of the samples were measured on a Horiba evolution high-resolution Raman spectrometer. The excitation wavelength is 325 nm and the scanning range is $100\text{--}2000\text{ cm}^{-1}$.

A Shimadzu UV3600 UV-Vis spectrophotometer was used to characterize the UV-Vis diffuse reflectance spectroscopy (DRS) optical properties of the sample at room temperature with BaSO₄ as a reference.

The photoluminescence spectrum (PL) of the sample was measured on the Shimadzu RF-5300IPC fluorescence spectrometer. A little barium sulfate was sprinkled on the bottom of the sample box, then the sample was put in the sample box and compacted. The excitation light wavelength is settled to be 300 nm, and the fluorescence wavelength was changed from 350 to 600 nm. The relationship between its energy intensity and the wavelength were measured to obtain the photoluminescence spectrum.

The transient photocurrent curves were performed on the CHI660E electrochemical workstation of Shanghai Chenhua Instrument Co., Ltd. with a standard three-electrode system with 0.5 M Na₂SO₄ solution as electrolyte, Ag/AgCl electrode as reference electrode, and 1 cm \times 1 cm platinum electrode as counter electrode. The preparation method of the

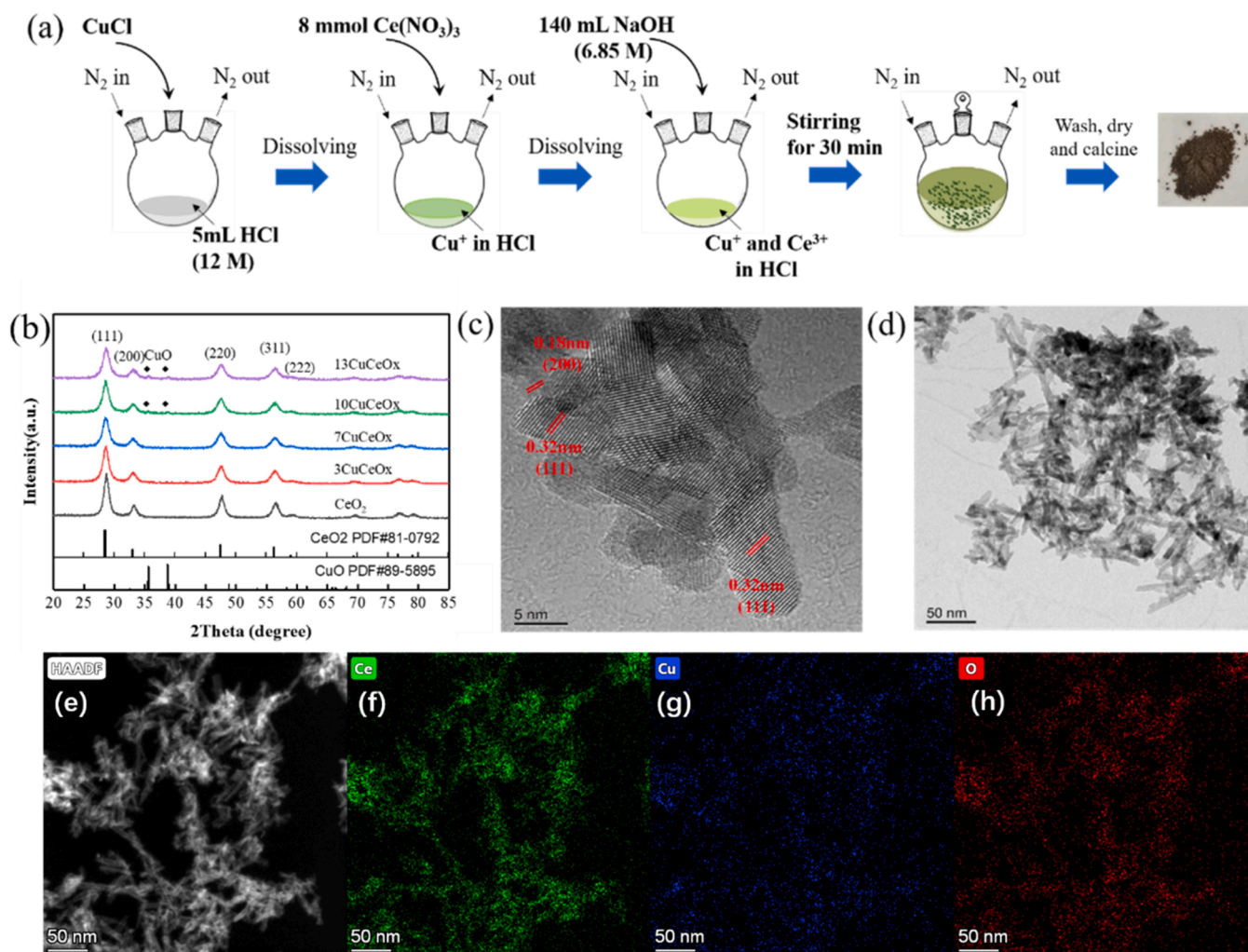


Fig. 1. (a) Synthetic route of CuCeO_{2-x} nanorods. (b) XRD spectra of CuCeO_{2-x} nanorods catalysts with different copper content. (c-d) HRTEM images and (e-h) EDX elemental distribution mapping images of 10CuCeO_x nanorods.

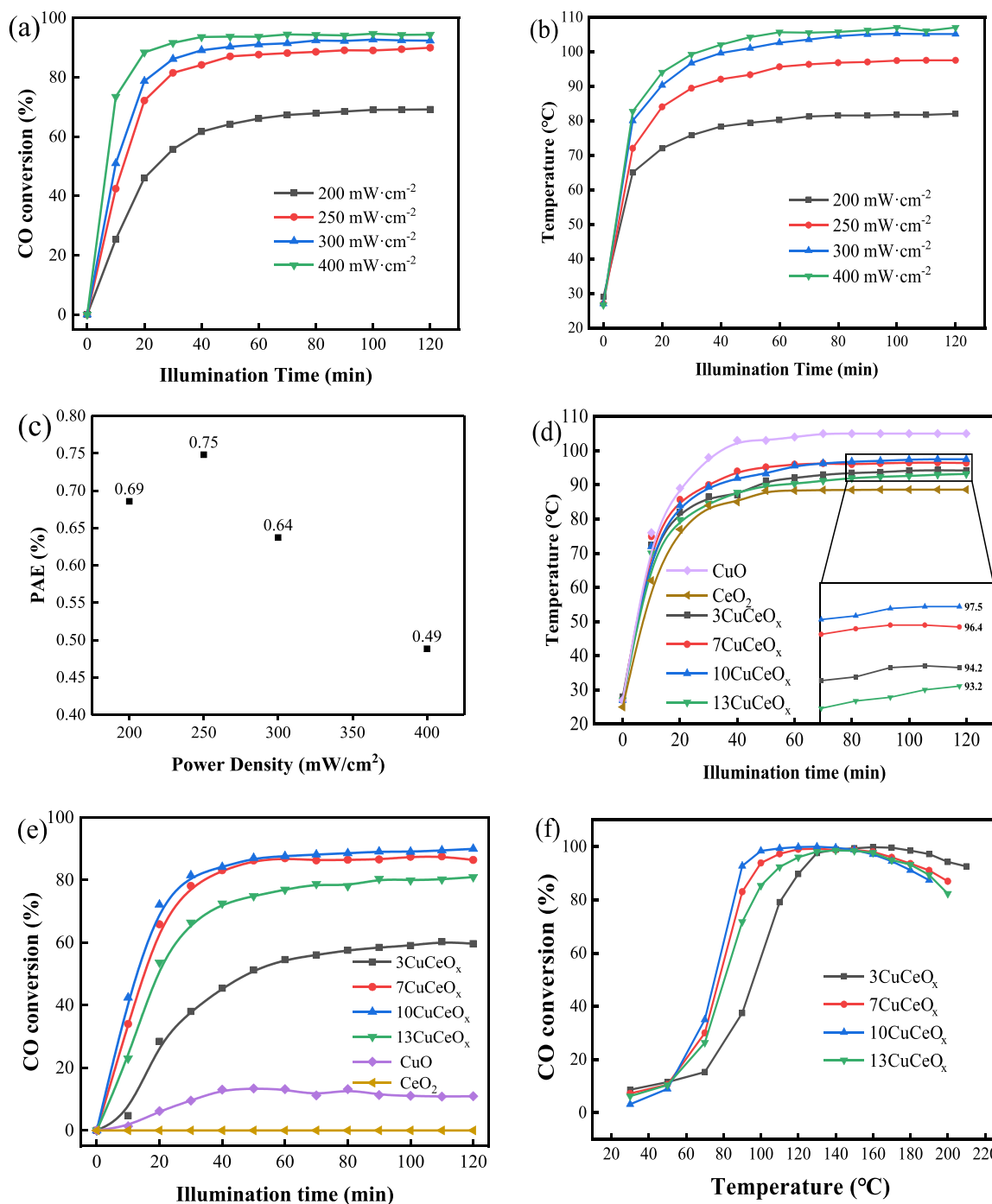


Fig. 2. (a) CO conversion of 10CuCeO_x in CO-PROX at different illumination power density. (b) Temperature curve of 10CuCeO_x at different illumination power density. (c) Apparent photoactivation efficiency of 10CuCeO_x in CO-PROX at different illumination power density. CO conversion of 10CuCeO_x in CO-PROX at different space velocity at 250 mW·cm⁻² (d) Temperature curves and (e) CO conversion of CuCeO_{2-x} nanorods with different copper amount in CO-PROX at 250 mW·cm⁻² (Reaction condition: 0.5%CO/0.5%O₂/25%H₂ + Ar; WHSV : 60000 mL·h⁻¹·g_{cat}⁻¹). (f) The thermocatalytic CO conversion of CuCeO_{2-x} nanorods with different copper amount.

working electrode is as follows: N-methyl-1-pyrrolidone was used as the solvent. 5 mg of the sample was ultrasonically dispersed in 1 mL of ethanol with 100 μ L of PVDF solution (10 mg/mL) for 30 min to obtain a working electrode spin-coating solution. The 2 cm * 2 cm fluorine-doped indium tin oxide (FTO) conductive glass (Ying Kou OPV Tech Co. Ltd., China) was ultrasonically cleaned with acetone, ethanol, and deionized water for 15 min, and then dried at 100 °C. After sealing the glass with insulating tape leaving only a corner of 1 cm * 1 cm, 50 μ L of working electrode solution was dropped on the glass and spin coated at 2000 r/

min for 30 s on the KW-4A desktop homogenizer (produced by the Institute of Microelectronics, Chinese Academy of Sciences). After drying for 15 min at 100 °C, the above spin-coating drying operation was repeated for 10 times. After removing the insulating tape, the glass with working electrode spin-coating solution was placed in a muffle furnace at 100 °C for 24 h to obtain a working electrode. The working electrode was soaking in sodium sulfuric acid electrolyte for 24 h before testing. The light source adopts the Xenon light source of Zhongjiao Jinyuan Technology Co., Ltd. with the light intensity of 250 mW·cm⁻², and the

photocurrent test is performed alternately between light and dark at an interval of 20 s

2.4. Catalytic performance

Photothermal catalytic Activity in CO-PROX: The photothermal CO preferential oxidation reaction of the catalyst was carried out in a self-made flow quartz reactor. 0.1 g of the sample was dispersed on the sand core with a diameter of 4 cm in the reactor. A xenon light source directly illuminates the catalyst from the upper side through the quartz window. The light intensity of the sample is controlled by adjusting the distance of the light source and the catalyst, and the light component is adjusted through the device filter. In addition, the side wall is also connected with a thermocouple inserted into the catalyst layer to detect temperature changes in real time. The feed gas with the total flow velocity of 100 sccm and the composition of 25% H₂ + 0.5% O₂ + 0.5% CO and Ar in balance passed through the catalyst. The outlet gas passes through a cold trap to remove the water in it, and then was separated by the column for separation, and finally reaches the detector for concentration determination. Among them, O₂ is separated by a 5 Å molecular sieve separation column and detected by a TCD detector. After CO is separated by a PN separation column, it is converted into methane by a methane converter and then detected by an FID detector.

The conversion rate of carbon monoxide is calculated by the following formula (CO_{in} represents the CO concentration in the feed gas, and CO_{out} represents the CO concentration in the product):

$$CO_{conversion} = \frac{CO_{in} - CO_{out}}{CO_{in}} \times 100\%$$

The selectivity of oxygen to carbon monoxide is calculated by the ratio of carbon monoxide oxygen consumption to total oxygen consumption (O_{2 in} represents the O₂ concentration in the feed gas, O_{2 out} represents the O₂ concentration in the product):

$$O_2_{selectivity} = \frac{0.5(CO_{in} - CO_{out})}{O_{2 in} - O_{2 out}} \times 100\%$$

Thermocatalytic Activity in CO-PROX: The thermal catalytic activity in CO-PROX is carried out in a self-made system. 100 mg catalyst of 60–80 mesh was diluted with 40–60 mesh quartz sand in equal volume, and placed in the middle of the quartz reactor. The thermocouple at the middle end of the catalyst bed was placed to accurately measure reaction temperature. The catalyst was first pretreated at 150 °C for 30 min in a 10% O₂/Ar atmosphere to remove surface contaminants. After it is naturally cooled to room temperature, the feed gas with the total flow velocity of 100 sccm and the composition of 50% H₂ + 1% O₂ + 1% CO and Ar in balance, is introduced. The detection of the outlet gas and the calculation methods of CO conversion and O₂ selectivity are the same with that in the photothermal CO preferential oxidation reaction. In addition, the same feed gas composition of 25% H₂ + 0.5% O₂ + 0.5% CO and Ar in balance were doped to compare the photothermal and thermal catalysis performance of 10CuCeO_x sample.

3. Results and discussion

3.1. Texture and structure properties of CuCeO_{2-x} nanorods

Compared with the traditional synthetic method of CeO₂ nanorods that usually proceeded at high temperature (100 °C) and long duration (24 h) [22,23], from the synthetic route of CuCeO_{2-x} nanorods (Fig. 1 (a)), the current co-precipitation temperature of the mixed nanorods kept at 30 °C and its reaction time was controlled only 30 min. The CuCeO_{2-x} nanorods obtained by this simple and fast preparation method behaves as the rod morphology with the diameter of 5 nm and the length of 70–80 nm (Fig. 1(b)), which exposed with {111} and {200} facets (Fig. 1(c)). It can be seen that the signals of Ce, Cu and O uniformly distribute in the EDX mapping images (Fig. 1(e-h)), indicating

the high distribution between copper and ceria species in 10CuCeO_x. The ICP-MS results demonstrate the weight fraction of Cu in the series CuCeO_{2-x} nanorods catalysts were 3.0%, 7.0%, 9.6% and 14.6% respectively for 3CuCeO_x, 7CuCeO_x, 10CuCeO_x and 13CuCeO_x, which further confirm the elemental composition and content of CuCeO_{2-x} nanorods catalyst. In addition, the XRD patterns show all the CuCeO_{2-x} nanorods with different copper dopant amount have the characteristic diffraction peaks of cubic fluorite CeO₂, and there arises the diffraction peaks of monoclinic CuO in the catalyst as the copper content reaches to 10%, indicating the high dispersion of copper oxide entities on the CuCeO_{2-x} nanorods with copper content no more than 7% and the agglomeration of the large-grained CuO nanoparticles separated out of CuCeO_{2-x} nanorods with excess copper dopant. The XRD Rietveld refinements were accomplished by using the Maud software. The anisotropic size function and Popa rules for which the broadening of the crystallite size is ascribed to a linear combination of spherical harmonic functions were set to be the method of refining crystallite size and morphology of the basic grain. The basic grain sizes are 7.6, 6.7, 6.2, 6.1 and 6.0 nm respectively for CeO₂, 3CuCeO_x, 7CuCeO_x, 10CuCeO_x and 13CuCeO_x. According to our previous research [24], the growth mechanism of ceria nanorod follows to the oriented attachment of the cube-like basic grains with a [110] growth direction and the subsequent Ostwald ripening. The grain size of the cube-like basic grain is equal to the diameter of the nanorod. The reduced tendency of the basic grain size indicates the Cu species is enriched near grain boundaries of ceria, hindering grain boundary movement and thus preventing grain growth. N₂ adsorption-desorption isothermal curves (Fig. S3 and Table S1) indicates S_{BET} and pore volume values of CuCeO_{2-x} nanorods reduced with the more copper dopant, causing by the agglomeration of the large-grained CuO nanoparticles.

3.2. Photothermal catalytic performance of CuCeO_{2-x} nanorods

The as-synthesized CuCeO_{2-x} nanorods were configured on the self-made photothermal gas-solid catalysis reactor (Fig. S2) and the CO-PROX catalytic performance were tested under different illumination conditions. As shown in Fig. 2(a) and (b), the CO conversion and reaction temperature of 10CuCeO_x were positively correlated with the illumination power density, which remarkably enhanced as the power density increased from 200 to 250 mW·cm⁻² but only slightly lifted as the power density further increased to 400 mW·cm⁻². We calculated the apparent photoactivation efficiency (PAE) of 10CuCeO_x in CO-PROX at different illumination power densities based on the CO conversion in photothermal catalysis and E_a (the activation energy in thermal catalysis, Fig. S3), as shown in Fig. 2(c). The PAE value at 250 mW·cm⁻² is the largest among the four different illumination conditions, which means that excessive photon injection results in loss of optical efficiency and heat loss of the reactor. Moreover, to evaluate the effect of the residing time on the catalytic performance of CuCeO_{2-x} nanorods, other different WHSV parameters including 30000 and 120000 mL·h⁻¹·g_{cat}⁻¹ were also tested for photothermal CO-PROX at 250 mW·cm⁻² (see Fig. S4). When the WHSV over 10CuCeO_x catalyst was increased from 60000 to 120000 mL·h⁻¹·g_{cat}⁻¹, the photothermal CO conversion drops from 90% to 70%. A decrease of WHSV diminished from 60000 to 30000 mL·h⁻¹·g_{cat}⁻¹ gave rise to the constant CO conversion of 90% for 10CuCeO_x catalyst. Therefore, the photothermal catalytic activity of CuCeO_{2-x} nanorods with different copper amount were tested under 250 mW·cm⁻² with the space velocity of 60000 mL·h⁻¹·g_{cat}⁻¹.

As shown in Fig. 2(d), under the simulated solar illumination, the surface temperature of CuCeO_{2-x} nanorods quickly increased to about 70 °C and then shows some discrepancy, which reaches from 94.2 to 97.5 °C and reduces to 93.2 °C as the copper amount increased from 3% to 10% and 13% respectively. The discrepancy of the surface temperature indicates the different photo-to-thermal conversion efficiency of the series of catalyst, which might depend on their light absorption capacity. As a result, 10CuCeO_x exhibits the highest CO conversion of 90% in the

Table 1

Surface elements distribution, the ratio of Cu^+ in Cu, A_{584}/A_{454} and hydrogen consumptions of the reduction peaks of CuCeO_{2-x} nanorods with different copper content.

Catalyst	Surface composition (at%)				Cu/ (Cu+Ce) (%)	Cu^+ in Cu (%)	Ce^{3+} in Ce (%)	$A_{584}/$ A_{454}	α peak		β peak		γ peak		Total H_2 cons. ($\mu\text{mol/g}$)
	Cu2p	Ce3d	O1s	Cl1s					peak temp. ($^{\circ}\text{C}$)	H_2 cons. (mmol/ g)	peak temp. ($^{\circ}\text{C}$)	H_2 cons. (mmol/ g)	peak temp. ($^{\circ}\text{C}$)	H_2 cons.	
3CuCeO _x	4.06	13.52	44.05	38.37	23.1	33.74	15.6	0.57	169	282	192	628	196	126	910
7CuCeO _x	5.54	11.1	43.09	40.27	33.3	34.86	16.4	0.59	157	484	181	830	210	376	1440
10CuCeO _x	6.12	12.03	43.08	38.77	33.7	37.45	17.3	1.01	169	878	196	670	220	844	1924
13CuCeO _x	6.13	11.09	43.63	39.15	35.6	29.57	17.1	0.93	173	1016	201	656			2517

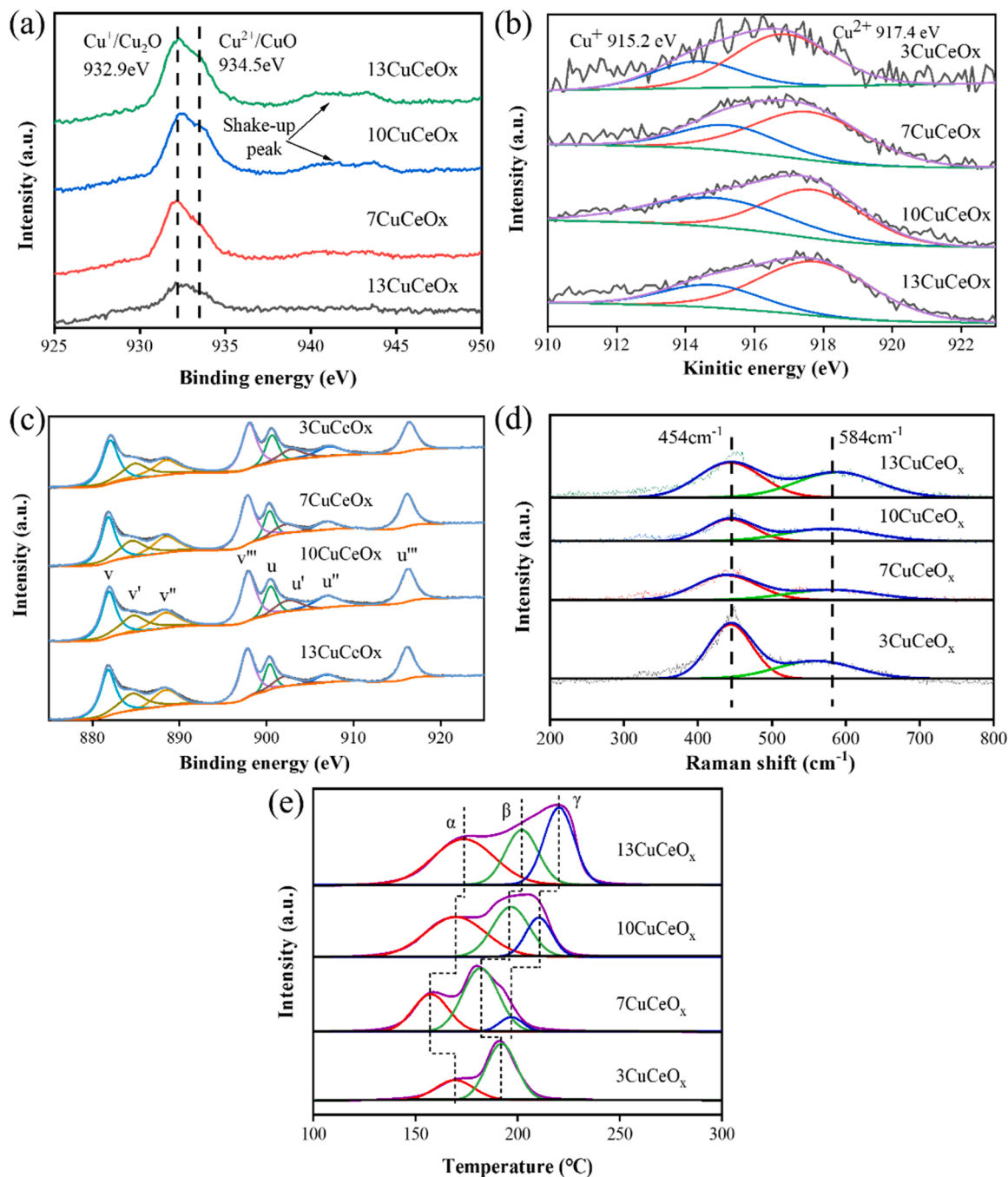


Fig. 3. XPS spectra (a: Cu 2p 3/2 b: CuLMM c: Ce 3d), UV-Raman spectra (d) and H_2 -TPR profile (e) of CuCeO_{2-x} nanorods with different copper amount.

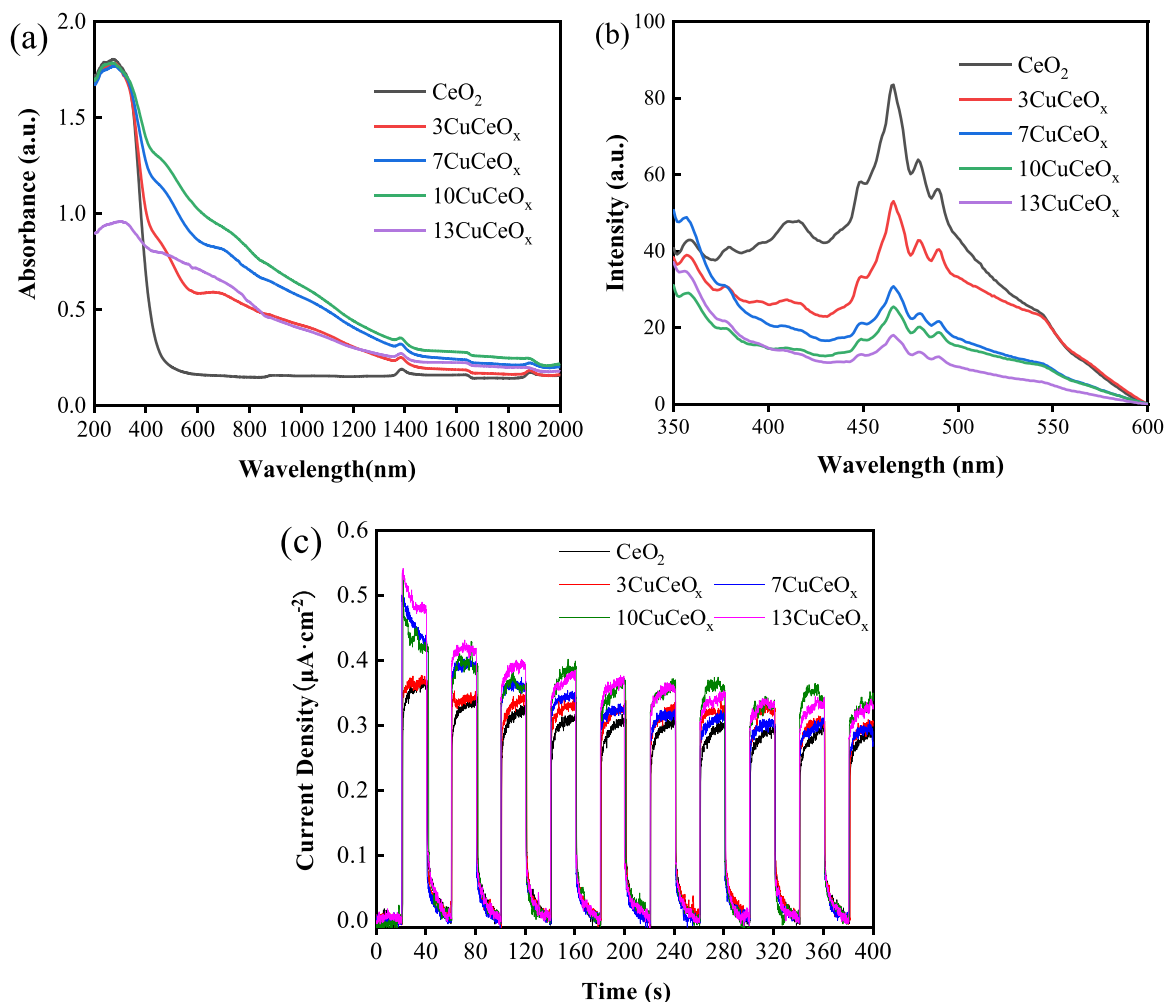


Fig. 4. (a) UV-Vis-IR absorption spectra (200–2000 nm). (b) Photoluminescence spectra under 330 nm excitation. (c) The transient photocurrent curves of CuCeO_{2-x} nanorods.

photothermal CO-PROX, which is respectively $\sim 50\%$ and 10% higher than 3CuCeO_x and 13CuCeO_x (Fig. 2(e)). Turnover frequency (TOF) represents the intrinsic activity of the catalyst. The TOF values of the series catalysts are calculated to be 0.00033, 0.00030, 0.00031 and 0.00013 s^{-1} respectively for 3CuCeO_x , 7CuCeO_x , 10CuCeO_x and 13CuCeO_x , which indicates the intrinsic activity of CuCeO_{2-x} nanorods basically remains unchanged as the copper content increased from 3% to 10% and the enhanced CO conversion is attributed to the increased active sites. However, for 13CuCeO_x , the decreased TOF value is mainly due to the agglomeration of copper species to bulk phase CuO that shows low activity for CO-PROX. In addition, the temperatures and CO conversion of the pure CuO and CeO_2 under the simulated solar illumination were also presented in Fig. 2(d) and (e). The surface temperature of CeO_2 is the lowest with the CO conversion of zero. Although much higher photo-thermal temperature arises on the surface of pure CuO than that of the composite CuCeO_{2-x} nanorods, the weaker CO oxidation ability of the former indicates the significant contribution of the synergistic Cu-Ce interaction for the CO-PROX process. From the thermal CO-PROX performance of the series catalysts in Fig. 2(f), the photo-thermal and thermal CO conversion are basically conforming with the similar variation trend along with the increased copper amount. The relationship between the photothermal and thermal CO-PROX performance of CuCeO_{2-x} nanorods in photothermal CO-PROX reflects that the photothermal catalytic activity is closely related to the photo-to-thermal conversion efficiency and Cu-Ce synergistic interaction of CuCeO_{2-x} nanorods catalyst. The former greatly dominates the surface

temperature of the active species and reaction temperature of the gas molecular, and the latter affects the generation and transformation of active Cu and O species. Therefore, on the purpose to figure out the decisive factors of CuCeO_{2-x} nanorods in photothermal CO-PROX, the characterization and discussion relevant to the Cu-Ce synergistic interaction and the photo-to-thermal conversion ability were mainly carried out in the next two sections from the aspects of the element distribution/redox property and optical properties of the catalysts.

3.3. Elements distribution and redox property

As a general consensus mentioned in many literatures [24–27], the amount of surface distributed copper species and its valence state, the oxygen vacancy concentration of copper-ceria catalyst are regarded the key parameters affecting the strengthen of Cu-Ce interaction. The surface element distributions and valence state of Cu, Ce, O species were obtained by XPS spectra and the oxygen vacancy concentration of CuCeO_{2-x} nanorods were characterized by UV-Raman spectra. As shown in Table 1, the surface Cu content (represented by the atomic ratio of $\text{Cu}/(\text{Cu}+\text{Ce})$) alters to larger values along with the more copper species doping into ceria nanorods, however, the increasing tendency seems to slow down as the Cu content larger than 7%. This phenomenon means a large portion of the redundant copper species were packaged in the insider of the catalyst that could not be detected by XPS spectra (the detection depth is only $\sim 10\text{ nm}$), which indicates the agglomeration of CuO particles with larger grain size, as in accordance with XRD results.

Fig. 3(a) and (b) present the Cu 2p 3/2 and Cu L3VV spectra and the ratios of Cu^+ in Cu derived from Cu L3VV were present in Table 1. The increased density of the Cu 2p 3/2 peaks at the range of 931–935 eV indicates the increased surface copper content. The incremental relative intensity between the peak of $\text{Cu}^{2+}/\text{CuO}$ at the binding energy of 934.5 eV and that of $\text{Cu}^+/\text{Cu}_2\text{O}$ and the occurrence of the shake-up peaks at the range of 940–945 eV also demonstrates the agglomeration of CuO particles as the copper dopant amount larger than 7%. The ratios of Cu^+ in Cu of the series catalysts were derived from the Cu L3VV (Table 1), and Cu^+ is generally regarded as the active copper species generated from the Cu-Ov-Ce structure and functions to adsorb CO molecular and formed $\text{Cu}^+\text{-CO}$ intermediates. The gradually elevated ratio of Cu^+ in Cu along with the copper dopant amount from 3% to 10% indicates the much stronger Cu-Ce interaction, until the copper dopant amount to 13%. In general, the reduction of Ce^{4+} to Ce^{3+} is accompanied by the generation of oxygen vacancies. Fig. 3(c) shows the Ce3d XPS spectra of CuCeO_{2-x} nanorod. The Ce3d spectrum of each catalyst contains two series of spin-orbit multiplets of u and v. The characteristic peaks attributed to Ce^{4+} include six peaks are the three main peaks of Ce3d3/2 corresponding to the u series (peaks u (900.6–901.0 eV), u' (907.5–907.7 eV) and u''' (916.6–916.9 eV)), and three main peaks of the v series (v (882.2–882.6 eV), v' (889.1–889.3 eV) and v''' (898.2–898.5 eV)). The characteristic peaks attributed to Ce^{3+} include the two peaks of u' (903.5–904.2 eV) and v' (885.1–885.8 eV) [28]. The relative content of Ce^{3+} in cerium species was obtained by calculating the ratio of the peak area assigned to Ce^{3+} to the total peak area of cerium species. As listed in Table 1, the content of Ce^{3+} on the surface of CuCeO_{2-x} nanorods shows an ascending tendency as the copper content increased from 3% to 10% and slightly reduced with 13% copper content. This results further evidence that the copper dopant affects the oxygen vacancy content due to the incorporation of copper ions into ceria lattice with the interfacial structure of $\text{Cu}^+\text{-Ov-Ce}^{3+}$ [29]. The area ratio between the two bands respectively at 584 cm^{-1} (oxygen vacancies in the ceria lattice that arouse the non-degenerate LO mode) and 454 cm^{-1} (the F2g variation mode of the cubic fluorite structure phase) [30] in UV-Raman spectra (Fig. 3(d)) is an indicator for the oxygen vacancy concentration on the surface of CuCeO_{2-x} nanorods. The increased oxygen vacancy concentration (Table 1) is mainly caused by the incorporation of copper ions into the lattice of ceria lattice, which is conducive to the generation of strong Cu-Ce interaction in 10CuCeO_x .

The redox property of copper-ceria catalysts mainly affected by the dispersion state of copper species and the interaction strengthen between copper and ceria species. for instance, in the H_2 -TPR profile of CuCeO_{2-x} nanorods (Fig. 3(e)), the highly dispersed copper species make contribution to the reduction peak α with the lowest reduction temperature that is the easiest to be reduced by hydrogen. The interfacial Cu-Ov-Ce species which is much harder to be reduced results in the reduction peak of β and the crystal phase CuO grains contributes to the reduction peak of γ [6,29]. The hydrogen consumption of peak γ matches to the amount of crystal phase CuO grains detected by XRD and XPS. The higher hydrogen consumption of peak α represent more highly dispersed copper oxide entities and the strengthened reducibility. The changed reduction temperature of peak α might is caused by the size of the copper oxide entities. The peak β is mainly influenced by interfacial Cu-Ov-Ce species, whose structure and quantity are specifically related with the types and amount of highly dispersed copper oxide entities and the oxygen vacancy. Overall considering the results about the elements distribution, the oxygen vacancy concentration and the data of H_2 -TPR listed in Table 1, the copper-ceria interaction in 7CuCeO_x and 10CuCeO_x are relatively much stronger than the other two samples. The former is benefited by the smaller sized copper oxide entities with strong reducibility, and the latter owns to the more highly dispersed copper oxide entities and the high concentration of oxygen vacancy.

3.4. Optical characterization

CeO_2 is an n-type semiconductor with a band gap of 3.1 eV with the light absorption range of ultraviolet band. Nanostructured CuO is a p-type semiconductor with the narrow bandgap of 1.2 eV in bulk with the whole spectral response of sunlight. Therefore, the composite of copper oxide with ceria nanorods is certain to significantly affects the optical absorption, the charge separation and recombination of photogenerated electrons and holes of CuCeO_{2-x} nanorods catalyst. As shown in UV-Vis-IR absorption spectra of the catalysts (Fig. 4(a)), the strong light absorption in the ultraviolet range of 200–400 nm is attributed to the inherent inter-band absorption of ceria [31]. The optical absorption shifts from the ultraviolet (UV) to near infrared, which indicates the composition of copper oxide with ceria reduced the band gap of ceria and enhanced the full spectrum absorption along with the color of the sample changed from faint yellow to dark brown. The wide light adsorption region clearly suggested that the composite CuCeO_{2-x} nanorods catalyst could strongly harvest solar energy, and the electron-hole might be richly generated by the harvesting. The visible light absorption intensity of CuCeO_{2-x} nanorods catalyst shows an order of $10\text{CuCeO}_x > 7\text{CuCeO}_x > 13\text{CuCeO}_x > 3\text{CuCeO}_x > \text{CeO}_2$ and the UV light absorption intensity is in a sequence of $\text{CeO}_2 \approx 3\text{CuCeO}_x \approx 7\text{CuCeO}_x \approx 10\text{CuCeO}_x > 13\text{CuCeO}_x$. The inferior UV light response is caused by the agglomeration of bulk phase CuO grains that weakened the inherent absorption of cerium oxide. It should be noticed that the intensified visible light absorption is basically consistent with the detected temperatures of the catalysts and their photothermal CO-PROX catalytic activities with illumination, demonstrating the higher visible light absorption facilitate the photo-to-thermal conversion ability and the heating effect of CuCeO_{2-x} nanorods catalyst.

The charge separation property of the series samples was evaluated by the photoluminescence (PL) spectra (Fig. 4(b)). The emission intensity of PL decreased significantly with the composition of copper and ceria, and continued to decrease along with the higher copper content in CuCeO_{2-x} nanorods, indicating that the effectively suppressed electron-hole recombination. It is mainly attributed to the more efficient separation of the photogenerated carriers caused by the addition of copper that makes photogenerated electrons in the semiconductor CeO_2 transfer to Cu^{2+} as electron capture center and reduces the recombination of carriers [32]. The generation and separation efficiency of the photoinduced electron-hole pairs were also investigated by the on-off cyclic transient photocurrent experiment under full spectrum illumination at a fixed voltage of 0.5 V (Fig. 4(c)). The current response increases when light is illuminated and decreases when there is no light. This is due to the fact that the photogenerated carrier output by the semiconductor CeO_2 excited by light illumination. The delay of the photocurrent change should be mainly attributed to the storage and release of a small amount of charge in CeO_2 nanorods such as surface defects. After doping with copper species, the photocurrent response of CuCeO_{2-x} nanorods electrode changes significantly. Specifically, the photocurrent response basically increments with the higher copper doping amount from 3% to 13% for the first cycle, indicating the intensified generation and separation efficiency of the photoinduced electron-hole pairs in CuCeO_{2-x} nanorods. However, as the light charging and discharging process gradually gets balanced in the following illumination/dark cycles, the photocurrent response shows a reduced tendency and becomes steady at the sequence of $13\text{CuCeO}_x \approx 10\text{CuCeO}_x > 7\text{CuCeO}_x \approx 3\text{CuCeO}_x > \text{CeO}_2$. The highest photocurrent intensity of 13CuCeO_x and 10CuCeO_x indicates the most efficient electron-hole separation/transfer, whereas which is not exactly in accordance with their photothermal catalytic activities. The charge separation property of the series CuCeO_{2-x} nanorods verified by PL spectra and transient photocurrent curves indicates that the generation and recombination of the photo-induced carriers is not the decisive factors that affects the catalytic performance of CuCeO_{2-x} nanorods in photothermal CO-PROX.

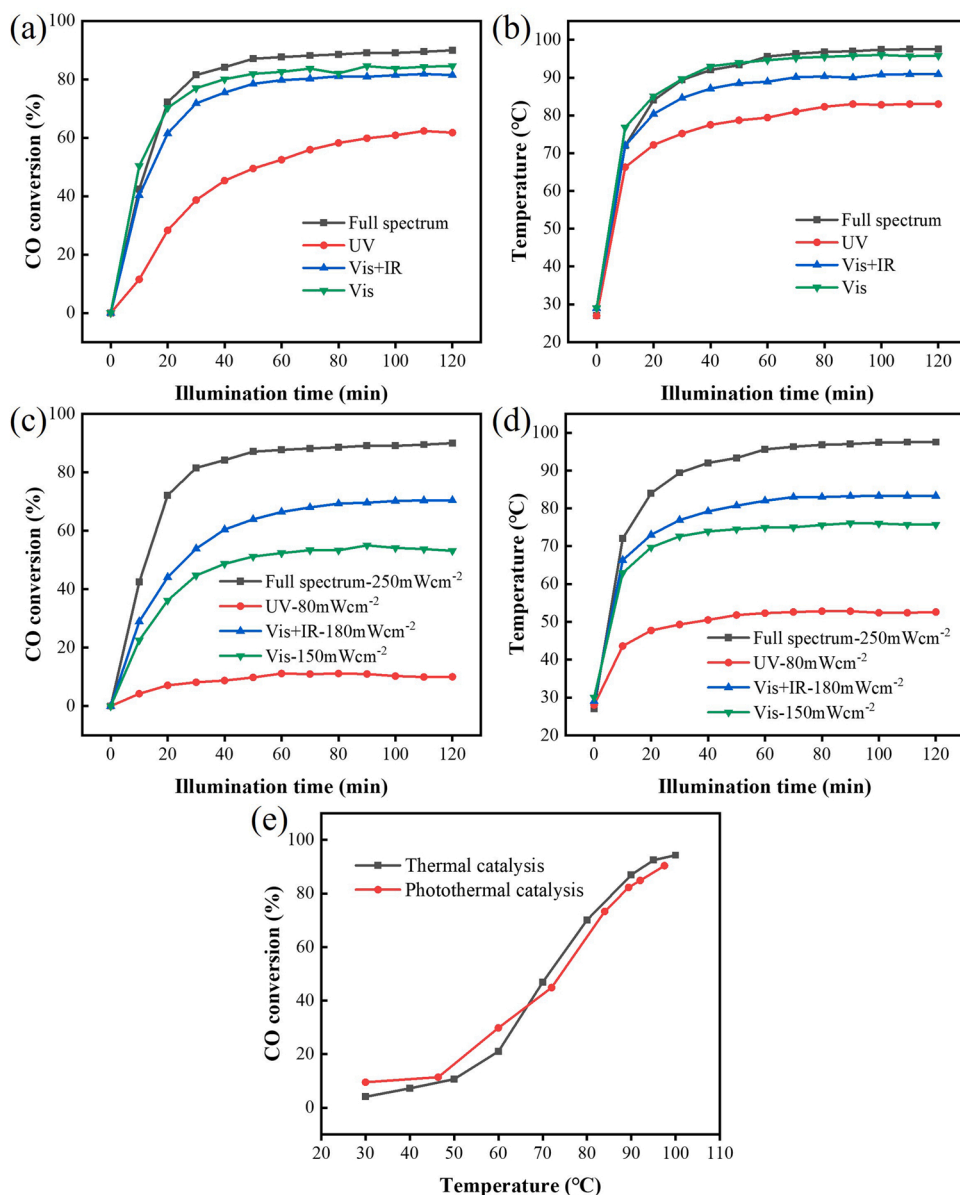


Fig. 5. (a) CO conversion and (b) Temperature curve of 10CuCeO_x illuminated under different optical composition with the same power density of 250 mW·cm⁻². (c) CO conversion and (d) Temperature curve of 10CuCeO_x illuminated under different optical compositions obtained by types of filters of the full spectra with the total density of 250 mW·cm⁻². (e) Comparison of CO conversion curves of 10CuCeO_x under the same temperature stimulated by the thermal catalysis and photothermal catalysis.

4. Discussion on photothermal catalysis over Cu-Ce catalysts

In general, the photothermal catalysis reaction could be broadly divided into three categories. One is photocatalysis and thermocatalysis in series mode. The second is a light-driven thermocatalytic reaction, in which light only serves as a heat source (In terms of reaction mechanism, the essence of the reaction is a thermocatalytic process). The third is the thermally assisted photocatalytic reaction. On the purpose to further verify the reaction mode of CuCeO_{2-x} nanorods in photothermal CO-PROX, a control experiment was designed to study the contributions of the different light composition of CuCeO_{2-x} affected the activity of photothermal catalytic CO-PROX reaction that closely related to the creation of photocarriers and photo-to-thermal conversion ability. Fig. 5 (a) and (b) respectively show the CO conversion and temperature curves of 10CuCeO_x illuminated under different optical composition with the same power density of 250 mW·cm⁻². The catalytic activity of 10CuCeO_x under different irradiation conditions was basically proportional to the reached temperature: full spectrum (90%, 97 °C) > Vis (82%, 95 °C) > UV (60%, 82 °C). It means that compared with the single visible light or UV light, the full spectrum illumination exhibits the much

higher heating effect and make higher contribution to the CO oxidation on 10CuCeO_x under the same illumination density. Moreover, the heating effect of visible light on 10CuCeO_x is much stronger than the UV light, which may be caused by the creation of photocarriers not only the photo-to-thermal conversion under the UV light irradiation.

Fig. 5(c) and (d) respectively present the CO conversion and temperature curve of 10CuCeO_x illuminated under different optical compositions obtained by types of filters of the full spectra (the power densities of full spectra, Vis+IR, Vis and UV are respectively measured as 250, 180, 150 and 70 mW·cm⁻²). From the temperature curves and the correspond CO conversion under different irradiation conditions, the adsorption of visible light contributes the most heat energy and resulted in the highest CO conversion. The contribution of UV and IR light are rather weaker than the visible light neither in heating effect or the CO conversion. This phenomenon indicates CO conversion is quite closely related to the energy dispersion of full spectra and the characteristic light adsorption. Compared with UV and IR light, the wide and strong visible light absorption results in efficient photo-to-thermal conversion ability of 10CuCeO_x.

Moreover, in order to justify the contribution of photocatalysis and

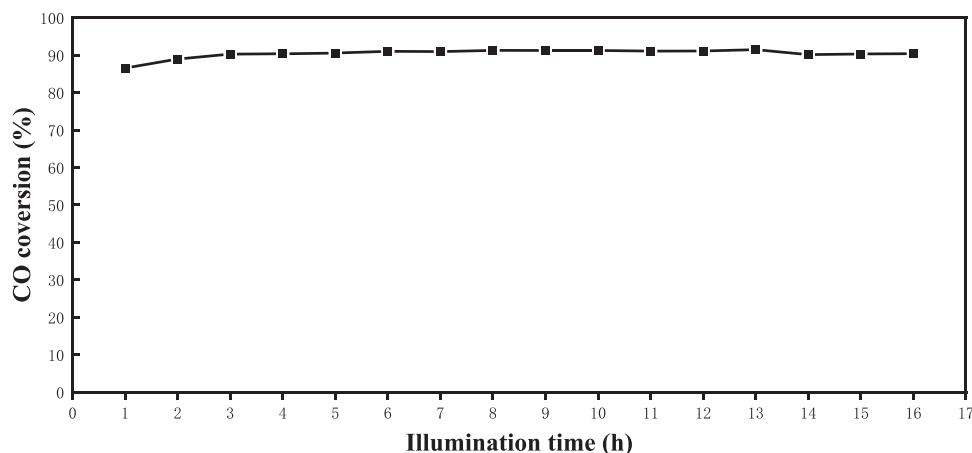


Fig. 6. CO conversion curves of 10CuCeO_x in long term photothermocatalytic stability test for CO-PROX at 250 mW·cm⁻² (Reaction condition: 0.5%CO/0.5%O₂/25%H₂ + Ar ; WHSV : 60000 mL·h⁻¹·g_{cat}⁻¹).

thermal catalysis to the total photothermal CO oxidation activity, the comparison of CO conversion curves of 10CuCeO_x under the same temperature stimulated by the thermal catalysis and photothermal catalysis is displayed in Fig. 5(e). As the temperature is relative lower (< 70 °C), the photothermal CO conversion is always higher than the pure thermal CO conversion, indicating the participation of the photocatalysis process under simulated solar light irradiation besides the thermal catalysis caused by the photo-to-thermal conversion. However, as the temperature is elevated to higher than 70 °C, the CO conversion of thermal catalysis and photothermal catalysis is rather approximate to each other and the latter is even slightly inferior than the former. It means that the photothermal CO conversion almost totally origins from the thermal catalysis process that owns to the photo-to-thermal effect of CuCeO_{2-x} nanorods under light irradiation, and the contribution of photocatalysis process scarcely existent at high reaction temperature because of the fast recombination of the photoinduced electron-hole pairs, which exactly explains the discrepancy between the charge separation property and the corresponding photothermal catalytic activities of CuCeO_{2-x} nanorods with different copper amount.

5. Long term photothermocatalytic stability of CuCeO_{2-x} nanorods

The long term photothermocatalytic stability of 10CuCeO_x has been tested and the result is shown in Fig. 6. It can be seen that the CO conversion maintains at 90% for 16 h and shows no downward trend, which indicates that 10CuCeO_x exhibits pretty good photothermal stability. In addition, TEM images, XRD patterns and XPS spectra of the used-10CuCeO_x catalyst are performed and exhibited in Figs. S8–10. Compared with the fresh sample, the used-10CuCeO_x catalyst basically maintain the nanorods morphology, however, the length of nanorods dramatically decreased to 20–30 nm and even some nanoparticles are formed. It means that the 10CuCeO_x nanorods get broken to some degree under the reducing atmosphere and illumination of the long-term photothermal catalytic test condition. According to the XRD patterns of the fresh and used 10CuCeO_x catalyst, the characteristic diffraction peaks of ceria with cubic fluorite structure are well maintained and the intensity of the characteristic diffraction peaks of bulk phase CuO shows a little decreased. It indicates that the redispersion of bulk phase CuO might occurs under the long-term photothermal catalytic test condition, which exists as small CuO nanoparticles that could not be detected by XRD. Furthermore, the reduced ratio of Cu/(Cu+Ce) also indicates the redispersion of bulk phase CuO that causes diminished surface copper content. On the other hand, compared with the fresh sample, the ratio of Cu⁺ and Ce³⁺ are both increased under the reducing reaction atmosphere of long term stability test. The former is the active center for CO

adsorption and the latter facilitates the oxygen mobility, which benefits the stable CO oxidation capability of 10CuCeO_x catalyst.

6. Conclusion

In summary, Cu doped CuCeO_{2-x} nanorods catalysts were synthesized with a fast and simple coprecipitation method at the room temperature, and were applied for photothermal CO-PROX under UV–vis–IR light irradiation. The photothermal catalytic activity of CuCeO_{2-x} nanorods doped with 10 wt% Cu reaches to 90% CO conversion under Xe lamp illumination (2.5 suns), and the solar driven photothermal CO-PROX reaction on CuCeO_{2-x} nanorods were proposed to be proceeded by the light-to-thermal conversion and subsequently to drive a thermal catalytic process. The catalytic performance of CuCeO_{2-x} nanorods in photothermal CO-PROX is closely related to the photo-to-thermal conversion efficiency and Cu-Ce synergetic interaction of CuCeO_{2-x} nanorods catalyst. The former greatly dominates the surface temperature of the active species and reaction temperature of the gas molecular, and the latter affects the generation and transformation of active Cu and O species. The introduction of CuO_x greatly broaden the optical absorption range and promotes the light absorption capacity of ceria nanorods, which induces the catalyst with high photo-to-thermal conversion capability. Moreover, the optimal copper dopant benefits to enhance the Cu-Ce synergetic interaction and accelerate the oxidation reaction taking place at low temperature. CuCeO_{2-x} nanorods catalyst shows promising competitive activity and ultra-low cost compared with the noble-based catalyst for the purification of hydrogen streams by the clean and eco-friendly sunlight sources.

CRediT authorship contribution statement

Xaolin Guo: Project administration, Supervision, Formal analysis, Data curation, Writing – original draft. **Wangxiang Ye:** Conduct experiments, Formal analysis, Data curation, Writing – original draft. **Ziang Chen:** Auxiliary experimenter. **Ang Zhou:** Auxiliary experimenter. **Dingfeng Jin:** Research collaborator. **Tingli Ma:** Supervision, Project administration, Formal analysis, Data curation.

Declaration of Competing Interest

The authors declare that they have no known competing financial interests or personal relationships that could have appeared to influence the work reported in this paper.

Acknowledgements

We gratefully acknowledge the financial supports from Natural Science Foundation of Zhejiang Province (No. LQ21B030012).

Appendix A. Supporting information

Supplementary data associated with this article can be found in the online version at doi:10.1016/j.apcatb.2022.121334.

References

- [1] S.F. Cao, Y.Y. Zhao, S. Lee, S.Z. Yang, J.L. Liu, G. Giannakakis, M.W. Li, M. Y. Ouyang, D.W. Wang, E.C.H. Sykes, M. Flytzani-Stephanopoulos, High-loading single Pt atom sites [Pt-O(OH)_x] catalyze the CO PROX reaction with high activity and selectivity at mild conditions, *Sci. Adv.* 6 (2020), <https://doi.org/10.1126/sciadv.aba3809>.
- [2] D.I. Potemkin, E.Y. Filatov, A.V. Zadesenets, A.M. Gorlova, N.A. Nikitina, D. A. Pichugina, A comparative study of CO preferential oxidation over Pt and Pt_{0.5}Co_{0.5} nanoparticles: Kinetic study and quantum-chemical calculations, *Mater. Lett.* 260 (2020), <https://doi.org/10.1016/j.matlet.2019.126915>.
- [3] G. Xiang, S. Zhao, C. Wei, C. Liu, H. Fei, Z. Liu, S. Yin, Atomically dispersed Au catalysts for preferential oxidation of CO in H₂-rich stream, *Appl. Catal. B* 296 (2021), 120385, <https://doi.org/10.1016/j.apcatb.2021.120385>.
- [4] J. Chen, C.L. Wang, C.C. Zong, S. Chen, P.C. Wang, Q.W. Chen, High catalytic performance of Au/Bi₂O₃ for preferential oxidation of CO in H₂, *ACS Appl. Mater. Interfaces* 13 (2021) 29532–29540, <https://doi.org/10.1021/acsami.1c04644>.
- [5] X. Guo, Z. Qiu, J. Mao, R. Zhou, Shape-controlled Cu_xCe_{1-x}O₂ nanorods catalyst and the active components functioned in selective oxidation of CO in hydrogen-rich stream, *J. Power Sources* 451 (2020), 227757, <https://doi.org/10.1016/j.jpowsour.2020.227757>.
- [6] X. Guo, W. Ye, T. Ma, Investigation of the re-dispersion of matrix Cu species in Cu_xCe_{1-x}O₂ nanorod catalysts and its effect on the catalytic performance in CO-PROX, *Catal. Sci. Technol.* 10 (2020) 4766–4775, <https://doi.org/10.1039/D0CY00519C>.
- [7] Z. Qiu, X. Guo, J. Mao, R. Zhou, Elucidating the structure, redox properties and active entities of high-temperature thermally aged CuO_x-CeO₂ catalysts for CO-PROX, *PCCP* 23 (2021) 15582–15590, <https://doi.org/10.1039/D1CP01798E>.
- [8] Z. Qiu, X. Guo, J. Mao, R. Zhou, New design and construction of abundant active surface interfacial copper entities in Cu_xCe_{1-x}O₂ nanorod catalysts for CO-PROX, *J. Phys. Chem. C* 125 (2021) 9178–9189, <https://doi.org/10.1021/acs.jpcc.1c02030>.
- [9] T.M. Nyathi, N. Fischer, A.P.E. York, M. Claeys, Environment-dependent catalytic performance and phase stability of Co₃O₄ in the preferential oxidation of carbon monoxide studied in situ, *ACS Catal.* 10 (2020) 11892–11911, <https://doi.org/10.1021/acscatal.0c02653>.
- [10] L. Zhong, M. Barreau, D. Chen, V. Caps, M. Haevecker, D. Teschner, D.H. Simonne, E. Borfecchia, W. Baaziz, B. Šmíd, S. Zafeirotas, Effect of manganese promotion on the activity and selectivity of cobalt catalysts for CO preferential oxidation, *Appl. Catal. B* 297 (2021), 120397, <https://doi.org/10.1016/j.apcatb.2021.120397>.
- [11] K. Yang, Y. Li, K. Huang, X. Chen, X. Fu, W. Dai, Promoted effect of PANI on the preferential oxidation of CO in the presence of H₂ over Au/TiO₂ under visible light irradiation, *Int. J. Hydrog. Energy* 39 (2014) 18312–18325, <https://doi.org/10.1016/j.ijhydene.2014.09.053>.
- [12] K. Yang, K. Huang, L. Lin, X. Chen, W. Dai, X. Fu, Superior preferential oxidation of carbon monoxide in hydrogen-rich stream under visible light irradiation over gold loaded hedgehog-shaped titanium dioxide nanospheres: Identification of copper oxide decoration as an efficient promoter, *J. Power Sources* 284 (2015) 194–205, <https://doi.org/10.1016/j.jpowsour.2015.03.003>.
- [13] Y. Zhang, Q. Li, C. Liu, X. Shan, X. Chen, W. Dai, X. Fu, The promoted effect of a metal-organic frameworks (ZIF-8) on Au/TiO₂ for CO oxidation at room temperature both in dark and under visible light irradiation, *Appl. Catal. B* 224 (2018) 283–294, <https://doi.org/10.1016/j.apcatb.2017.10.027>.
- [14] K. Yang, Y. Zhang, C. Meng, F. Cao, X. Chen, X. Fu, W. Dai, C. Yu, Well-crystallized ZnCo₂O₄ nanosheets as a new-style support of Au catalyst for high efficient CO preferential oxidation in H₂ stream under visible light irradiation, *Appl. Surf. Sci.* 391 (2017) 635–644, <https://doi.org/10.1016/j.apsusc.2016.07.006>.
- [15] K. Yang, C. Meng, L. Lin, X. Peng, X. Chen, X. Wang, W. Dai, X. Fu, A heterostructured TiO₂-C₃N₄ support for gold catalysts: a superior preferential oxidation of CO in the presence of H₂ under visible light irradiation and without visible light irradiation, *Catal. Sci. Technol.* 6 (2016) 829–839, <https://doi.org/10.1039/C5CY01009H>.
- [16] I. Barroso-Martín, A. Infantes-Molina, A. Talon, L. Storaro, E. Rodríguez-Aguado, E. Rodríguez-Castellón, E. Moretti, CO preferential photo-oxidation in excess of hydrogen in dark and simulated solar light irradiation over AuCu-based catalysts on SBA-15 mesoporous silica-titania, *Materials* 11 (2018), <https://doi.org/10.3390/ma11071203>.
- [17] E. Rodríguez-Aguado, A. Infantes-Molina, A. Talon, L. Storaro, L. León-Reina, E. Rodríguez-Castellón, E. Moretti, Au nanoparticles supported on nanorod-like TiO₂ as catalysts in the CO-PROX reaction under dark and light irradiation: effect of acidic and alkaline synthesis conditions, *Int. J. Hydrog. Energy* 44 (2019) 923–936, <https://doi.org/10.1016/j.ijhydene.2018.11.050>.
- [18] E. Rodríguez-Aguado, J.A. Cecilia, A. Infantes-Molina, A. Talon, L. Storaro, E. Moretti, E. Rodríguez-Castellón, Photocatalyzed preferential oxidation of CO under simulated sunlight using Au-transition metal oxide-sepiolite catalysts, *Dalton Trans.* 49 (2020) 3946–3955, <https://doi.org/10.1039/C9DT04243A>.
- [19] C. Zhou, L. Cheng, Y. Li, M. Zeng, Y. Yang, J. Wu, X. Zhao, Novel photoactivation promotes catalytic abatement of CO on CuO mesoporous nanosheets with full solar spectrum illumination, *Appl. Catal. B* 225 (2018) 314–323, <https://doi.org/10.1016/j.apcatb.2017.11.081>.
- [20] J. Xu, X. Li, X. Wu, W. Wang, R. Fan, X. Liu, H. Xu, Hierarchical CuO colloidsomes and their structure enhanced photothermal catalytic activity, *J. Phys. Chem. C* 120 (2016) 12666–12672, <https://doi.org/10.1021/acs.jpcc.6b03750>.
- [21] Y. Li, Q. Sun, M. Kong, W. Shi, J. Huang, J. Tang, X. Zhao, Coupling oxygen ion conduction to photocatalysis in mesoporous nanorod-like ceria significantly improves photocatalytic efficiency, *J. Phys. Chem. C* 115 (2011) 14050–14057, <https://doi.org/10.1021/jp202720g>.
- [22] H.-X. Mai, L.-D. Sun, Y.-W. Zhang, R. Si, W. Feng, H.-P. Zhang, H.-C. Liu, C.-H. Yan, Shape-selective synthesis and oxygen storage behavior of ceria nanopolyhedra, nanorods, and nanocubes, *J. Phys. Chem. B* 109 (2005) 24380–24385, <https://doi.org/10.1021/jp055584b>.
- [23] H. Wang, S. Luo, M. Zhang, W. Liu, X. Wu, S. Liu, Roles of oxygen vacancy and Ox- in oxidation reactions over CeO₂ and Ag/CeO₂ nanorod model catalysts, *J. Catal.* 368 (2018) 365–378, <https://doi.org/10.1016/j.jcat.2018.10.018>.
- [24] X. Guo, R. Zhou, Identification of the nano/micro structure of CeO₂(rod) and the essential role of interfacial copper-ceria interaction in CuCe(rod) for selective oxidation of CO in H₂-rich streams, *J. Power Sources* 361 (2017) 39–53, <https://doi.org/10.1016/j.jpowsour.2017.06.064>.
- [25] P.S. Barbato, S. Colussi, A. Di Benedetto, G. Landi, L. Lisi, J. Llorca, A. Trovarelli, Origin of high activity and selectivity of CuO/CeO₂ catalysts prepared by solution combustion synthesis in CO-PROX reaction, *J. Phys. Chem. C* 120 (2016) 13039–13048, <https://doi.org/10.1021/acs.jpcc.6b02433>.
- [26] A.R. Miranda Cruz, E.M. Assaf, J.F. Gomes, J.M. Assaf, Active copper species of co-precipitated copper-ceria catalysts in the CO-PROX reaction: an in situ XANES and DRIFTS study, *Catal. Today* 381 (2021) 42–49, <https://doi.org/10.1016/j.cattod.2020.09.007>.
- [27] W. Li, X. Shen, R. Zeng, J. Chen, W. Xiao, S. Ding, C. Chen, R. Zhang, N. Zhang, Constructing copper-ceria nanosheets with high concentration of interfacial active sites for enhanced performance in CO oxidation, *Appl. Surf. Sci.* 492 (2019) 818–825, <https://doi.org/10.1016/j.apsusc.2019.06.292>.
- [28] J. Fan, X. Wu, X. Wu, Q. Liang, R. Ran, D. Weng, Thermal ageing of Pt on low-surface-area CeO₂-ZrO₂-La₂O₃ mixed oxides: effect on the OSC performance, *Appl. Catal. B* 81 (2008) 38–48.
- [29] A. Chen, X. Yu, Y. Zhou, S. Miao, Y. Li, S. Kuld, J. Sehested, J. Liu, T. Aoki, S. Hong, M.F. Camellone, S. Fabris, J. Ning, C. Jin, C. Yang, A. Nefedov, C. Wöll, Y. Wang, W. Shen, Structure of the catalytically active copper-ceria interfacial perimeter, *Nat. Catal.* 2 (2019) 334–341, <https://doi.org/10.1038/s41929-019-0226-6>.
- [30] Y. Lee, G. He, A.J. Akey, R. Si, M. Flytzani-Stephanopoulos, I.P. Herman, Raman analysis of mode softening in nanoparticle CeO₂-δ and Au-CeO₂-δ during CO oxidation, *J. Am. Chem. Soc.* 133 (2011) 12952–12955, <https://doi.org/10.1021/ja204479j>.
- [31] C. Schilling, C. Hess, Real-time observation of the defect dynamics in working Au/CeO₂ catalysts by combined operando raman/UV-vis spectroscopy, *J. Phys. Chem. C* 122 (2018) 2909–2917, <https://doi.org/10.1021/acs.jpcc.8b00027>.
- [32] M. Wang, M. Shen, X. Jin, J. Tian, M. Li, Y. Zhou, L. Zhang, Y. Li, J. Shi, Oxygen vacancy generation and stabilization in CeO_{2-x} by Cu introduction with improved CO₂ photocatalytic reduction activity, *ACS Catal.* 9 (2019) 4573–4581, <https://doi.org/10.1021/acscatal.8b03975>.